

Advanced Characterisation of Pore Structure in Next-Generation Reactor Graphites

Bradley Moresby-White^a, Katie L. Jones^{a,*}, G. Peter Matthews^a, Giuliano M. Laudone^a

^a*Faculty of Science and Engineering, University of Plymouth, Plymouth, UK*

Abstract

Nuclear grade graphite

Keywords: keyword, keyword, keyword

1. Introduction

This is a citation.[1]

2. Methodology

2.1. Materials

Virgin graphite samples of two grades, IG-110 and IG-430, were supplied by Toyo Tanso Ltd™, Osaka, Japan. The properties of both grades are tabulated (Table 1).IG-110 is currently employed in the three existing HTGRs worldwide, while IG-430 is designed to deliver increased density, strength, and thermal conductivity for future applications.[2] (Table 1). Both grades comply with *ASTMD7219-19*, including the requirement for a minimum bulk density exceeding 1.7 g/cm³ [3] (Table 1).

2.2. Sample preparation

Cuboids were sub-sampled from the virgin graphite blocks, with dimensions of approximately 10mm x 10mm x 100mm. The sub-samples were further subsampled into cuboids of side lengths 7mm, providing 3 cuboids per grade. Samples were polished via SiC polishing pads up to a grit size of P5000, to minimise topographical variations induced by sample preparation that may cause artefacts during SEM imaging or low pressure gas adsorption [5, 4].Samples were sonicated in 2-propanol for 24h to remove any contaminants, particularly

the lubricant used in the machining process. Samples were then dried under vacuum for 12 h at 305±5 °C using the BELPREP-vac (MicrotracBEL, Japan) in order to remove any residual moisture introduced during the sonication process.

2.3. Micrograph generation

The JEOL™IT510 Scanning Electron Microscope was used in the generation of the contiguous set of individual micrographs from which the full composite is assembled. The *Image Montage* capability, within the JEOLInScope™package, performed this function. The system captures a number of micrographs, with the motorised stage moving the electron beam over the specified area with a set overlap, with the software adjusting stigmation, contrast, and brightness. Shifts in contrast and brightness were on the order of < 1% and thus negligible in affecting intensity threshold for the full composite. The full set of parameters selected are tabulated (Table 2).

Make sure to double check that figure for ACB

2.4. Composite assembly

The composite assembly (i.e., "stitching") stage, where the overlapping micrographs are assembled into a single image per sample, has a significant impact on the porosity values as incorrect fusion will misrepresent pore structures. A stitching method based on the phase correlation approach originally developed by Kuglin and Hines, amongst the most popular approaches to image registration, was selected and operated as a plug-in within ImageJ [6, 7]. This method represents a development of the original phase correlation method[7].

*Corresponding author.
Email address: katie.jones@plymouth.ac.uk (Katie L. Jones)

Table 1: Manufacturer dataset for IG-110 and IG-430 [4]

Grade	Coke source	Bulk density/g cm ³	Filler particle size/ μm	Tensile strength/MPa	Young's modulus/GPa	Thermal conductivity/W m ⁻¹ K ⁻¹
IG-110	Petrol	1.77	10	25	9.8	120
IG-430	Pitch	1.82	10	37	10.8	140

Table 2: Parameters for composite assembly captured with the JEOL IT510 SEM using Image Montage Mode

Parameters	Values
Magnification (\times)	1000
Resolution ($\mu\text{m}/\text{px}$)	0.1
Surface area per micrograph (μm^2)	12 288
Overlap (%)	10
Micrographs per sample (n)	196

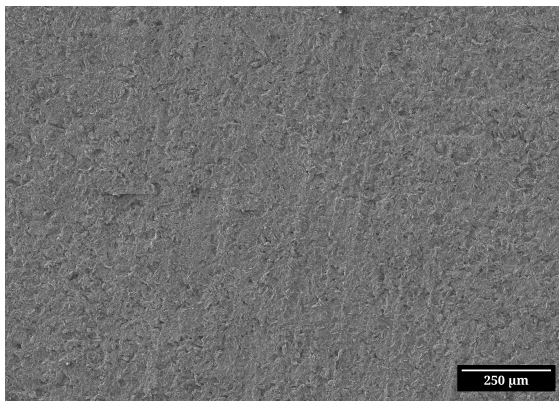


Figure 1: Fully assembled SEM composite: IG-430 Sample C, 1000 \times magnification, 5 kV accelerating voltage. Bar = 250 μm .

A key advantage of this method is the avoidance of error propagation by consecutive registration steps, which is key at this scale [7]. A further advantage is the sub-pixel accuracy of the fusion, as incorrect alignments would generate false pore diameters. The resulting composite micrographs showed excellent alignment with no visible delineation between individual micrographs, a relatively high FOV, high resolution, and clear distinction between porosity and bulk when examined closely (Figure 1).

2.5. Computation of Channel Porosity

2.5.1. Intensity/Greyscale Thresholding

Intensity thresholding, where intensity refers to the value of a given pixel in an 8-bit micrograph, is the core of global intensity thresholding. Intensity thresholding determines an intensity value at which porosity and bulk (i.e., foreground and background)

are distinguished. Intensity-based thresholding requires the conversion of the intensity values of the pixels in the micrograph into a histogram of intensity, enabling the selection of an image-wide threshold at which different classes can be separated.

For each 8-bit micrograph E (pixel values $0 \leq E(x, y) \leq 255$), we first compute its intensity histogram $H(i)$ for $i = 0, 1, \dots, 255$. Specifically,

$$H(i) = \sum_{x=1}^M \sum_{y=1}^N \mathbf{1}\{E(x, y) = i\},$$

where M and N are the image width and height (in pixels), and

$$\mathbf{1}\{E(x, y) = i\} = \begin{cases} 1, & \text{if the pixel at } (x, y) \text{ has intensity } i, \\ 0, & \text{otherwise.} \end{cases}$$

For each pixel, the equation checks the intensity and increments the count in the corresponding bin, yielding a 256-bin histogram whose entries $H(i)$ count the number of pixels at each intensity level.

Global automatic intensity thresholding algorithms optimising by different criteria to determine thresholds. For manual selection of a given threshold, or validation of an automatically selected threshold, there exists no certain criteria to allow a fully objective evaluation [8]. In this work, thresholding aims to select an intensity value that reliably binarizes porosity and bulk in a way that minimizes both Type I and II errors as evaluated by the operator (i.e., false positives, classifying a pore where one is not present, and false negatives, not classifying a pore where one is present).

A test of all 17 of the available automatic thresholding methods available in Fiji/ImageJ demonstrated that no automatic global intensity thresholding algorithm effectively distinguished between porosity and bulk with the sensitivity required to allow the classification of pores for the given histogram (Figure 2).

The key cause is likely the lack of a bimodal distribution in the histogram, meaning that there are statistically no classes to be separated, necessitating the use of a human-in-the-loop (HITL) approach.

need to make a figure for the histogram in ImageJ

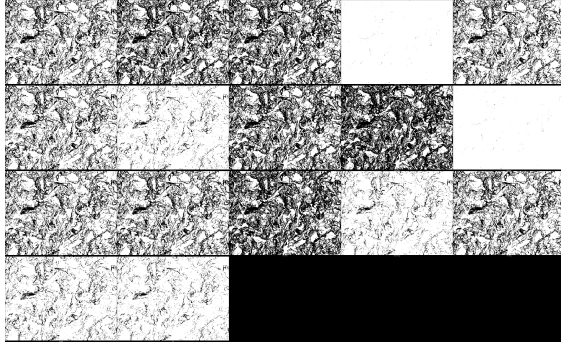


Figure 2: Thresholded Micrograph of IG-430 Sample C at 1000 \times Magnification. Methods are labelled sequentially from right to left, row by row. (a) Default (b) Huang (c) Huang2 (d) Intermodes (e) IsoData (f) Li (g) MaxEntropy (h) Mean (i) MinError(I) (j) Minimum (k) Moments (l) Otsu (m) Percentile (n) RenyiEntropy (o) Shanbhag (p) Triangle (q) Yen

A HITL (human-in-the-loop) approach was therefore undertaken, as illustrated in the process diagram through the example of IG-110 Sample B (Figure 3). Here, the operator subsamples the overall fused composite, then examines this subsample to determine the threshold at which the porosity and bulk are best separated. The operator then applies this threshold to the full composite, and the results are classified as either porosity or bulk to derive channel porosity.

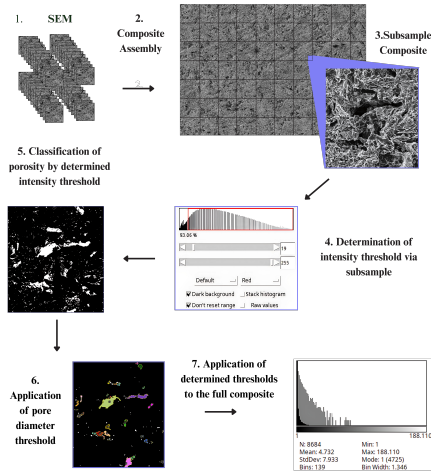


Figure 3: Full thresholding workflow detailing the process of micrograph generation, composite assembly, subsampling, intensity thresholding, and pore diameter thresholding.

Table 3: Effect of different pore area thresholds on IG-110 Sample B, showing the resulting pore count, average size, total area, and estimated channel porosity.

Area Threshold (μm^2)	0	0.5	1	2	4	8
Pore Count (n)	109	39	30	18	10	3
Average Size (μm^2)	1.709	4.437	5.554	8.263	12.611	29.003
Channel Porosity (%)	3.55	3.30	3.18	2.84	2.41	1.66

2.5.2. Pore Diameter Thresholding

Pore diameter thresholds are imposed in this work, as in previous works, to constrain the automated recognition of pores to that interval within which classification is deemed reliable [9, 8, 10]. The constraint on objectivity is the infeasibility of defining absolutely whether a given classification of a pore is correct. Even where this is done, at this scale it would require the comparison of classified porosity to the original micrograph, for thousands of pores per micrograph.

(Step 6, Figure 3) is the imposition of a pore size threshold via a HITL method once more, with the operator's comparison of the results of a range of pore diameter thresholds to the raw subsample to determine a specific area to be applied across the samples. The variations per threshold are shown in Table 3 and Figure 4.

Significant variation is exhibited in the number of pores characterised as a function of pore size threshold (Table 3). The corresponding variation in total porosity is lower, 3 pores of an area greater than 8 μm^2 in the subsample represent 46.71% of total porosity as classified, where no area threshold is applied. In this work, an area threshold of 1 μm^2 (dia = 1.12 μm) has been selected as the optimal compromise between the Type I and Type II errors.

2.6. Helium (He) Pycnometry

Skeletal density was obtained using a Pycnomatic ATC pycnometer (Thermo Fisher Scientific, Italy) at a temperature of $20.00 \pm 0.01^\circ\text{C}$. Measurements were taken in ten replicates per sample, calculating the arithmetic mean.

Solid phase volume V_{SOLID} was calculated assuming a theoretical density of $g \cdot \text{cm}^{-3}$ for an ideal graphite crystal. Closed Pore Volume (CPV) and Open Pore Volume (OPV) for each of the samples was calculated via equations 1 and 2.

$$\text{CPV} = \frac{m - V_{\text{SOLID}} \times \rho_s}{\rho_s} \quad (1)$$

$$\text{OPV} = V_{\text{BULK}} - \text{CPV} - V_{\text{SOLID}} \quad (2)$$

insert theoretical density here

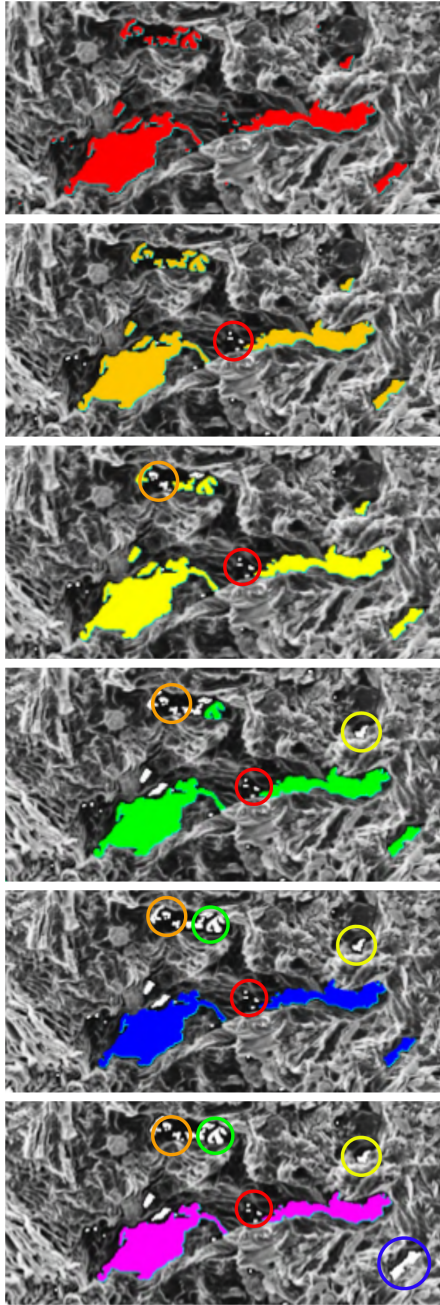


Figure 4: Effect of minimum area threshold on pore identification in subsample of IG-110 Sample B. Highlighted circles denote features which surpassed the previous threshold(s) only, indicated by colour. Thresholds applied (a-f, left-to-right, top-to-bottom): None, $0.5 \mu\text{m}^2$, $1 \mu\text{m}^2$, $2 \mu\text{m}^2$, $4 \mu\text{m}^2$, and $8 \mu\text{m}^2$.

Specific Pore Volume (SPV), the void volume accessible to helium per gram of sample was calculated via Equation 3.

$$\text{SPV} = \frac{1}{\rho} - \frac{1}{\rho_s} \quad (3)$$

2.7. Mercury (*Hg*) Intrusion Porosimetry

Mercury intrusion porosimetry operates on the fundamental principle that the pressure at which a non-wetting fluid intrudes a given pore is inversely proportional to the diameter of that pore (i.e., the larger the pore, the easier it is for the non-wetting fluid to enter it). The exact physical relationship between diameter and applied pressure is governed by the following equation (Eq. 4)

$$d = \frac{-4\gamma \cos \theta}{P} \quad (4)$$

The pore diameter d is calculated using the equation:

- d (m): Pore diameter
- γ (N/m): Surface tension of the fluid
- θ (degrees): Contact angle of the fluid with the surface
- P_{app} (P): Pressure

Values of 140° and 130° were used for advancing and receding contact angles respectively, while a value of 0.480 N m^{-1} was assumed for the surface tension of mercury [11].

Hg intrusion porosimetry cannot capture the full range of pore sizes as pores $> 89 \mu\text{m}$ diameter cannot be distinguished as mercury intrudes these pores without the application of a measurable amount of pressure, and thus the relation fails to yield a result (Eq. 4). For pores $> 2 \mu\text{m}$ diameter, structural damage due to the triaxial compression of the crystalline structure by intruded mercury precludes an accurate determination of porosity at this scale by *Hg* intrusion porosimetry [4]. Hence, the use of GCMC to "stitch" together the pore diameter ranges covered by both *Hg* and He adsorption. The pore size distribution (PSD) is generated by combining the methods into a single set of values, which PoreXpert inversely models to capture.

2.8. Nitrogen (N_2) Adsorption

Low-pressure gas adsorption isotherms were obtained using a BELSORP-max volumetric gas adsorption instrument (MicrotracBEL, Japan).

References

- [1] K. L. Jones, G. P. Matthews, G. M. Laudone, The effect of irradiation and radiolytic oxidation on the porous space of gilso-carbon nuclear graphite measured with mercury porosimetry and helium pycnometry, *Carbon* 158 (2020) 256–266. doi:<https://doi.org/10.1016/j.carbon.2019.11.084>. URL <https://www.sciencedirect.com/science/article/pii/S0008622319312175>
- [2] Toyo Tanso Co., Ltd., Atomic power and nuclear fusion, accessed April 21, 2025 (2025). URL <https://www.toyotanso.com/us/en/Products/application/atomic-nuclear.html>
- [3] ASTM International, D7219-19 Standard Specification for Isotropic and Near-isotropic Nuclear Graphites, published August 2019; supersedes D7219-08R14 (2019).
- [4] K. Jones, G. Laudone, G. Matthews, A multi-technique experimental and modelling study of the porous structure of ig-110 and ig-430 nuclear graphite, *Carbon* 128 (2018) 1–11. doi:[10.1016/j.carbon.2017.11.076](https://doi.org/10.1016/j.carbon.2017.11.076).
- [5] N. Fang, R. Birch, T. Britton, Optimizing broad ion beam polishing of zircaloy-4 for electron backscatter diffraction analysis, *Micron* 159 (2022) 103268. doi:[10.1016/j.micron.2022.103268](https://doi.org/10.1016/j.micron.2022.103268).
- [6] C. Kuglin, D. Hines, The phase correlation image alignment method, in: Proceedings of the International Conference on Cybernetics and Society, 1975, pp. 163–165.
- [7] S. Preibisch, S. Saalfeld, P. Tomancak, Globally optimal stitching of tiled 3d microscopic image acquisitions, *Bioinformatics* 25 (11) (2009) 1463–1465. arXiv:2009 Apr 3, doi:[10.1093/bioinformatics/btp184](https://doi.org/10.1093/bioinformatics/btp184).
- [8] Q. Huang, H. Tang, Porosity analysis of superfine-grain graphite ig-110 and ultrafine-grain graphite t220, *Materials Science and Technology* 35 (8) (2019) 962–968. doi:[10.1080/02670836.2019.1599557](https://doi.org/10.1080/02670836.2019.1599557).
- [9] J. Taylor, G. Hall, P. Mummery, Investigating the effects of stress on the pore structures of nuclear grade graphites, *Journal of Nuclear Materials* 470 (2016) 216–228. doi:[10.1016/j.jnucmat.2015.12.031](https://doi.org/10.1016/j.jnucmat.2015.12.031).
- [10] J. Kane, et al., Microstructural characterization and pore structure analysis of nuclear graphite, *Journal of Nuclear Materials* 415 (2) (2011) 189–197. doi:[10.1016/j.jnucmat.2011.05.053](https://doi.org/10.1016/j.jnucmat.2011.05.053).
- [11] J. Van Brakel, S. Modrý, M. Svatá, Mercury porosimetry: state of the art, *Powder Technology* 29 (1) (1981) 1–12. doi:[https://doi.org/10.1016/0032-5910\(81\)85001-2](https://doi.org/10.1016/0032-5910(81)85001-2). URL <https://www.sciencedirect.com/science/article/pii/S0032591081850012>